Producing spin-polarized photoelectrons by using the momentum gate in strong-field ionization experiments

Kunlong Liu, Klaus Renziehausen, and Ingo Barth*
Max Planck Institute of Microstructure Physics, Weinberg 2, 06120 Halle (Saale), Germany
(Received 5 April 2017; published 13 June 2017)

The ionization of the prealigned nitric oxide molecule by strong circularly polarized laser fields is studied via theoretical simulations of the spin-resolved photoelectron momentum distributions by solving numerically the three-dimensional time-dependent Schrödinger equation. Due to the spin-orbit entanglement in the ground state of nitric oxide and the sensitivity of the tunnel ionization of its doubly degenerate valence $2\pi_\pm$ orbitals carrying opposite electron ring currents to the sense of the laser-field rotation, the momentum-resolved spin-polarized photoelectrons are produced. We show that the spin polarization exhibits strong dependence on the kinetic energy as well as the emitting angle of the photoelectron. In addition to the laser control, the momentum gate in strong-field experiments would enable full control of the spin polarization.

DOI: 10.1103/PhysRevA.95.063410

I. INTRODUCTION

As a fundamental process in attosecond physics, tunnel ionization of atoms and molecules is the primary step towards a variety of strong-field phenomena such as high-order-harmonic [1–4] and attosecond-pulse generation [5–7], nonsequential double ionization [8,9], electron localization in molecular dissociation [10–12], laser-induced electron diffraction [13–16], multielectron dynamics [17–21], and so on. Having such an important role, tunnel ionization itself has attracted continuous investigations [22–26]. For example, low-energy structure in photoelectron spectra [27,28] and tunneling time [29–32] have been extensively studied in the past decade. Recently, the spin dynamics of the photoelectron released from noble-gas atoms by nonadiabatic tunnel ionization has been introduced into the realm of attoscience [33–35]. The underlying physics of producing spin-polarized photoelectrons and its potential applications, ranging from probing the magnetic properties on surfaces [36] to detecting the molecular chirality [37,38] at subfemtosecond time scales, have been attracting increasing interest.

In 2013, it was predicted in theory that the tunnel ionization of the valence p shell of noble-gas atoms by strong circularly polarized (CP) laser fields could produce spin-polarized photoelectrons [33]. The spin polarization of the photoelectron is a result of the spin-orbit couplings in the ionic states $|P_{3/2}\rangle$ and $|P_{1/2}\rangle$ of a noble-gas atom and the sensitivity of ionization in circularly polarized laser fields to the sense of the initial electron rotation in current-carrying valence p orbitals [39–43]. However, due to fourfold degeneracy of the ionic ground state $|P_{3/2}\rangle$, the spin polarization can reach only up to 50%. Integrated over both ionic $|P_{3/2}\rangle$ and $|P_{1/2}\rangle$ states, the spin polarization would decrease even further [33]. In a landmark experimental study by Hartung *et al.* [35], up to 30% spin polarization depending on the photoelectron kinetic energy was observed.

To achieve a higher degree of spin polarization of the photoelectron from noble-gas atoms, the ionization channel to the ionic state $|P_{1/2}\rangle$ needs to be separated from that to the $|P_{3/2}\rangle$ state in the experiment. Alternatively, highly spin polarized photoelectrons can be produced from the linear molecule, e.g., nitric oxide (NO) [44,45]. In contrast to noble-gas atoms (excluding helium) which have closed p shells and zero net spin in the ground state but open shells in ionic states, NO has an open valence π shell with only one electron but a closed shell after the removal of the valence electron, making the physical process for production of spin-polarized photoelectrons simpler. The ground state of NO is degenerate and has spin-orbit coupling. It splits into two doubly degenerate states, $|\Pi_{1/2}\rangle$ and $|\Pi_{3/2}\rangle$, separated by an energy of about 120 cm^{-1} (0.015 eV). The selection of the ground state $|\Pi_{1/2}\rangle$ of NO, on which we will focus in the present study, can be done in the molecular-beam experiment [46]. The NO molecule in this ground state has two equally possible electron configurations, $2\pi_+^\downarrow$ and $2\pi_-^\uparrow$, in the valence shell; that is, the valence electron of the current-carrying $2\pi_+$ ($2\pi_-$) orbital has spin down (up). Our previous study [44] showed that, in general, the ionization yield of the counterrotating π orbital with respect to the rotation of the strong CP laser pulse is higher than that of the corotating one. Due to different ionization rates for rotating $\pi_\pm$ orbitals in CP laser fields, as illustrated in Fig. 1, strong right-CP laser pulses remove more spin-up photoelectrons from the ground state $|\Pi_{1/2}\rangle$ of NO. Therefore, the production of photoelectrons with controllable spin polarization by strong CP laser fields is feasible.

Generally, the momentum-integrated spin polarization of the photoelectron cannot have very large values except for weak and fast-rotating CP laser fields. But the momentum gate for photoelectrons will provide potential access to achieve much higher spin polarization. It has been shown that the electrons removed from current-carrying atomic $p_\pm$ orbitals move and deflect differently [47,48]. The electron momentum and angular deflection are then mapped onto the photoelectron momentum distribution (PMD). We expect that the momentum drift and angular deflection can also be observed in PMDs for current-carrying molecular $\pi_\pm$ orbitals. Given that for NO the valence electron of the $2\pi_+^\downarrow$ orbital has spin opposite that of the $2\pi_-^\uparrow$ orbital, dislocation of the PMD peaks for these two orbitals would lead to the momentum-resolved

*barth@mpi-halle.mpg.de

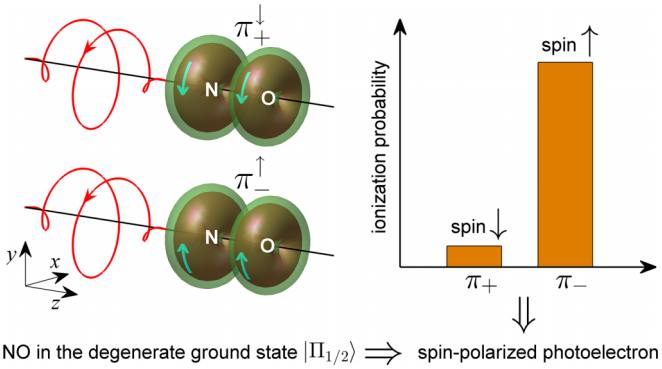

FIG. 1. The mechanism for the production of spin-polarized photoelectrons from the ground state $|\Pi_{1/2}\rangle$ of NO by circularly polarized laser pulses.

spin polarization of photoelectrons. So far, however, it is still a challenge to measure the momentum-resolved spin polarization of photoelectrons in experiments. In this paper, we theoretically simulate three-dimensional (3D) PMDs for the electron removed from the valence $2\pi_+^\downarrow$ and $2\pi_-^\uparrow$ orbitals of NO by a few-cycle circularly polarized laser pulse. Our results show that both 3D PMDs for $2\pi_+^\downarrow$ and $2\pi_-^\uparrow$ orbitals exhibit double-crescent structures but with observably different momentum drifts. We find that the streaks of the two-dimensional (2D) PMDs for these two orbitals are noticeably dislocated. By calculating the difference between the PMDs for spin-up and spin-down photoelectrons, momentum distributions for spin-polarized photoelectrons are obtained. We also show that the spin polarization strongly depends on both the kinetic energy and the emitting angle of the photoelectron and can reach more than 90% for very low kinetic energies or at certain emitting angles.

II. NUMERICAL CALCULATION

In the present work, we numerically solve the 3D time-dependent Schrödinger equation (TDSE) in the Cartesian coordinate system for the interaction between the NO molecule and the laser field. The molecule is prealigned along the z axis and perpendicular to the polarization plane of the laser pulse. Since the valence π shell of the NO molecule consists of only one electron, the single-active-electron approximation is applied in our calculations. Then, the length-gauge 3D TDSE for the single-electron wave function, $\Psi(\mathbf{r},t) = \Psi(x,y,z,t)$, within the dipole approximation is given by (atomic units are used unless stated otherwise)

$$i\frac{\partial}{\partial t}\Psi(\mathbf{r},t) = \left[-\frac{\nabla^2}{2} + V_0(\mathbf{r}) + \mathbf{r}\cdot\mathbf{E}(t)\right]\Psi(\mathbf{r},t), \qquad (1)$$

with $V_0(\mathbf{r})$ being the effective potential of NO [44]. The laser pulse used in our calculations is a right-CP laser pulse, and its electric field is given by

$$\mathbf{E}(t) = \mathcal{E}\sin^2\left(\frac{\pi t}{nT}\right)[\cos(\omega t)\mathbf{e}_x + \sin(\omega t)\mathbf{e}_y] \qquad (2)$$

for $t \in [0, nT]$, and otherwise, $\mathbf{E}(t) = \mathbf{0}$, where $\mathcal{E}$, ω, n, and $T = 2\pi/\omega$ are the electric field amplitude, the laser frequency, the number of laser cycles, and the period of one laser cycle, respectively.

The propagation of the wave function in Eq. (1) is performed using the split-operator Crank-Nicolson method with five-point finite differences on a nonuniform grid. The general procedure follows the method introduced in Ref. [49]. The general formulas for the finite-difference coefficients on the nonuniform grid are derived in the Appendix. During the time evolution of the wave function, the unphysical reflections at boundaries of the calculation box are avoided by using the split function that separates smoothly the outgoing wave packet. This wave packet is then propagated analytically by using the Volkov Hamiltonian and then contributes coherently to the final wave function $w(\mathbf{p},t_{\rm end})$ in the momentum space [50,51]. After the pulse is off, the propagation of the wave function continues for an additional 5 fs, so that the ionized wave packet is well separated from the bound wave packet. At the end of the propagation ($t = t_{\rm end}$), the wave packet in the area $|\mathbf{r}| < 80$ a.u. is eliminated with a smooth absorber. The remaining part of the wave function is then transferred from the position space to the momentum space. Finally, the transformed wave function is coherently added to $w(\mathbf{p},t_{\rm end})$. The final PMD is calculated as $Y(\mathbf{p}) = |w(\mathbf{p},t_{\rm end})|^2$.

In our simulation, the box ranges from -346.1 to 346.1 a.u. for the x and y dimensions and from -138.1 to 138.1 a.u. for the z dimension. The step sizes are $\Delta x = 0.13$ a.u. for $|x| < 14$ a.u., and otherwise, $\Delta x = 0.39$ a.u., and the same is true for the y dimension. For convenience of the Message Passing Interface (MPI) programming, we adopt a fixed step size $\Delta z = 0.24$ a.u. for the z dimension. The time step $\Delta t = 0.02$ a.u. is used for time propagation.

III. RESULTS AND DISCUSSION

Figures 2(a) and 2(b) present the 3D PMDs $Y_\pm(\mathbf{p})$ for the electron released from the valence $2\pi_+^\downarrow$ and $2\pi_-^\uparrow$ orbitals of NO by a three-cycle ($n = 3$) right-CP laser pulse. Here, the subscripts $+$ and $-$ indicate the positive and negative electron angular momenta $+\hbar$ and $-\hbar$, respectively. Thus, they correspond to the corotating and counterrotating orbitals with respect to the CP laser pulse. The wavelength and the intensity of the pulse are 800 nm and 1.75×10^{14} W/cm^2 ($\mathcal{E} = 0.05$ a.u.), respectively. The electric field given by Eq. (2) reaches its maximum pointing to $-\mathbf{e}_x$ at $t = 1.5\,T$.

One can see that the 3D PMDs in Figs. 2(a) and 2(b) split into two similar crescent distributions. This is due to the nodal structure of the $2\pi_\pm$ orbital of NO and the fact that the destructive interference of the wave packets ionized from two nuclei leads to the minimum in the PMDs near $p_z = 0$ [52]. As we will discuss below, the double-crescent distribution provides an additional degree of control to obtain highly spin-polarized photoelectrons.

Another important feature of the PMDs in Figs. 2(a) and 2(b) is that two crescent distributions of $\pi_+^\downarrow$ exhibit a radius larger than that of $\pi_-^\uparrow$. This difference indicates that the ionization of the corotating $\pi_+^\downarrow$ orbital by the right-CP laser pulse results in a larger momentum drift. In our calculations, the peaks of the one-dimensional (1D) distributions depending on the radial momentum p_r, calculated

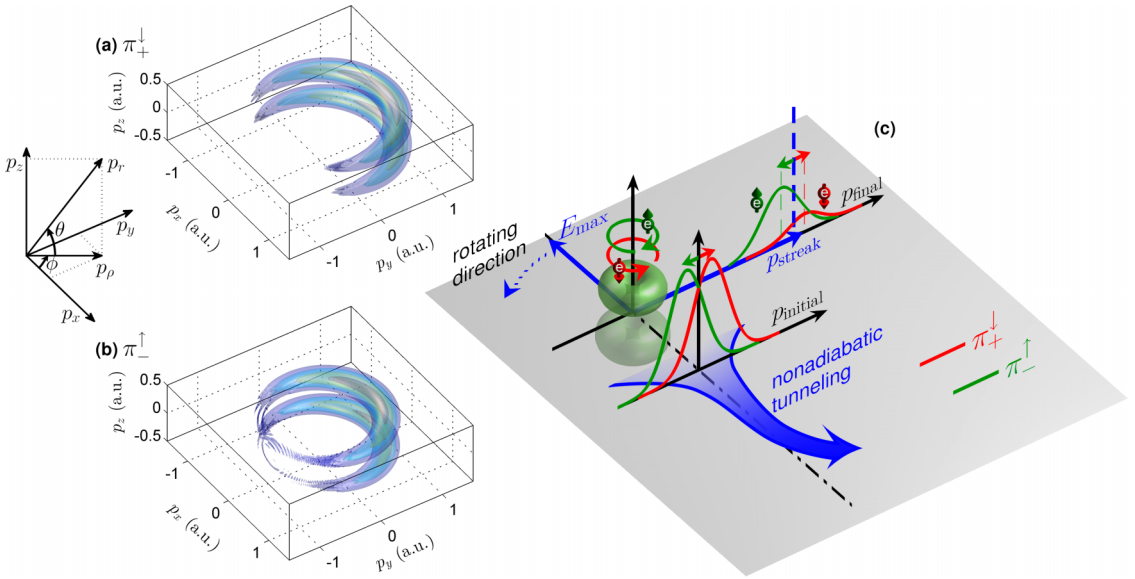

FIG. 2. The 3D PMDs for the electron released from the (a) valence $2\pi_+^\downarrow$ and (b) $2\pi_-^\uparrow$ orbitals of NO. These distributions are normalized to their maxima. The coordinate axes on the left side show the components of the photoelectron momentum vector. (c) The physical picture on the right side illustrates the ionization processes for these orbitals by a right-CP laser pulse.

as $Y_\pm^r(p_r) = p_r^2 \iint Y_\pm(\mathbf{p}) \cos\theta d\theta d\phi$, are at 1.04 and 0.88 a.u. for corotating $\pi_+^\downarrow$ and counterrotating $\pi_-^\uparrow$ orbitals, respectively. Meanwhile, the ionization ratio between π_- and π_+ orbitals is 3.16.

The underlying ionization processes for the $\pi_\pm$ orbitals can be explained in Fig. 2(c). When the electric field reaches its maximum pointing to $-\mathbf{e}_x$, the Coulomb potential on the opposite site is bent, and the electron will tunnel out of the nuclei through the rotating barrier. Since the π_+ electron rotates counterclockwise about the molecular axis, the electron released along the opposite direction of the electric field has an initial momentum $\mathbf{p}_{\text{initial}}$ pointing to $\mathbf{e}_y$, which is the same direction as the much larger momentum acquired from the electric field, denoted as $\mathbf{p}_{\text{streak}}$. In contrast, the direction of the initial momentum of the electron released from the π_- orbital is opposite that of $\mathbf{p}_{\text{streak}}$. Then, according to the "simple-man's theory," the final momentum drifts for the $\pi_\pm$ orbitals are given by $p_{\text{final}}^{(\pm)} = p_{\text{streak}} \pm p_{\text{initial}}$, indicating a larger momentum drift for the corotating π_+ orbital. In addition, due to the nonadiabatic effect on the ionization rate of current-carrying orbitals in the CP laser pulse, the yield of the photoelectron from the counterrotating π_- orbital is higher than that from the π_+ orbital [44], which is also illustrated in Fig. 2(c).

Next, let us focus on the spin polarization of the photoelectron after the strong-field tunnel ionization. Since the electron configurations $2\pi_+^\downarrow$ and $2\pi_-^\uparrow$ are equally distributed in the degenerate ground state $|\Pi_{1/2}\rangle$ of NO, both the spin-up and spin-down photoelectrons will be produced during the interaction of the ensemble of NO molecules with the CP laser pulse in the experiment. However, thanks to the different momenta and yields for the spin-up and spin-down photoelectrons, the momentum-resolved spin polarization of photoelectrons can be achieved by a strong CP laser field.

We present the 2D PMDs $Y_\pm^{x,y}(p_x, p_y) = \int Y_\pm(\mathbf{p}) dp_z$ in Figs. 3(a) and 3(b) and $Y_\pm^{\rho,z}(p_\rho, p_z) = \int Y_\pm(\mathbf{p}) d\phi$ in Figs. 3(d) and 3(e). Due to the electron configurations and the prealignment of the molecule, the PMDs Y_+ and Y_- for the

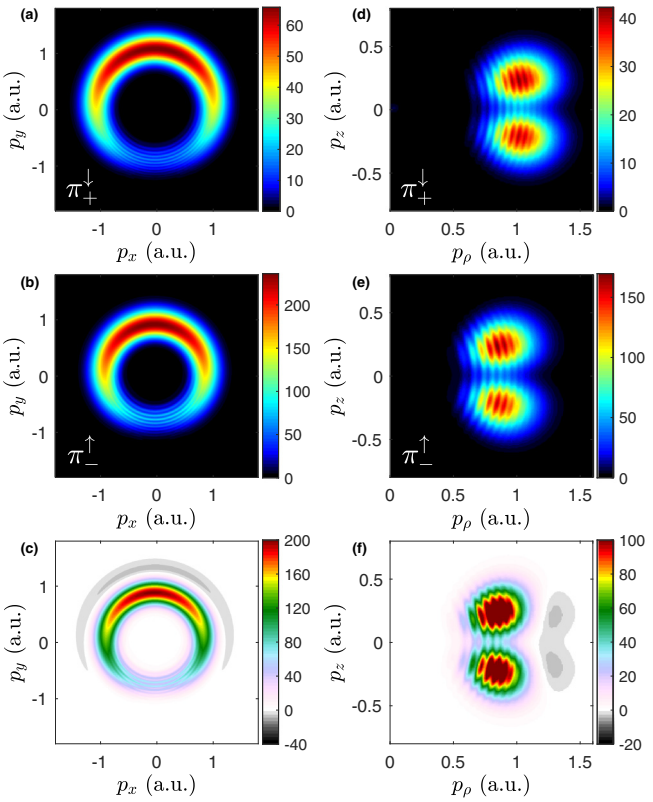

FIG. 3. The 2D PMDs for the photoelectrons released from the (a) and (d) valence $2\pi_+^\downarrow$ and (b) and (e) $2\pi_-^\uparrow$ orbitals of NO and (c) and (f) the momentum distribution of the spin-polarized photoelectrons; see Fig. 2 for the definition of the components of the photoelectron momentum vector.

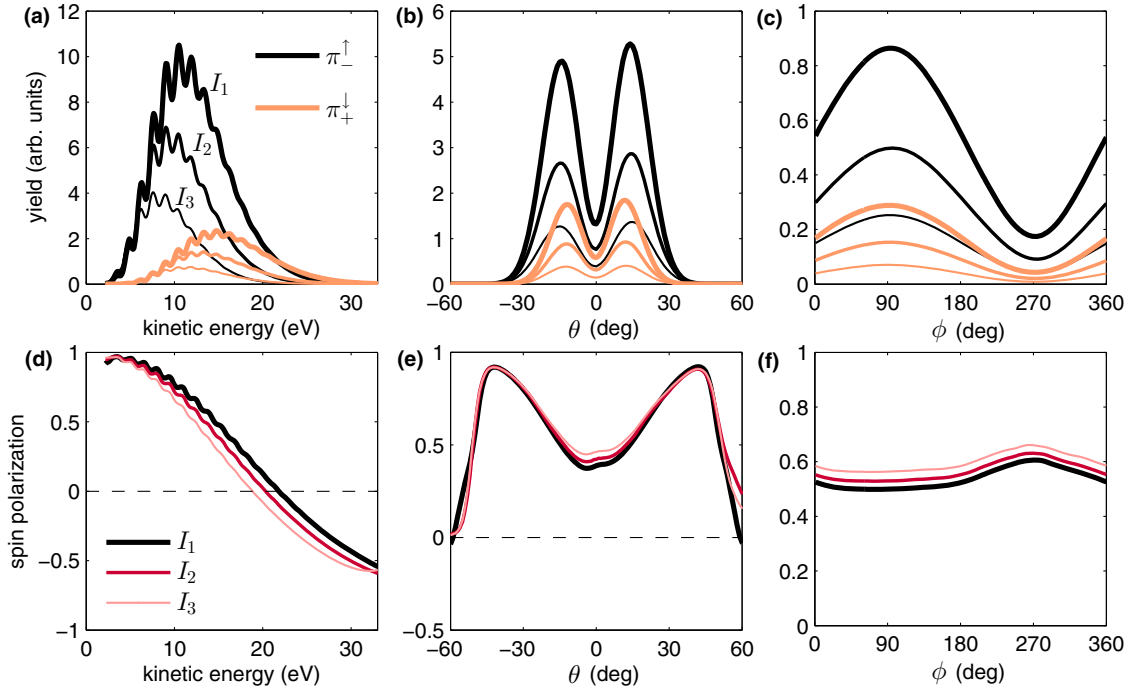

FIG. 4. The 1D distributions of the spin-up (black curves) and spin-down [orange (light gray) curves] photoelectrons as a function of (a) the photoelectron kinetic energy, (b) the elevation angle, and (c) the azimuthal angle. (d)–(f) The corresponding distributions of the spin polarization of photoelectrons. The thickness of the curves indicates the results for three different pulse intensities defined in the text.

ionization of the current-carrying π_+ and π_- orbitals are equivalent to the distributions $Y^\downarrow$ and $Y^\uparrow$ for the spin-down and spin-up photoelectrons, respectively [45]. By calculating the absolute asymmetry of the 2D PMDs for the spin-up and spin-down photoelectrons, defined as $\mathcal{A} = Y^\uparrow - Y^\downarrow$, we obtain the momentum distribution of the spin-polarized photoelectrons, as shown in Figs. 3(c) and 3(f). The positive and negative values of the absolute asymmetry $\mathcal{A}$ stand for the spin-up and spin-down polarizations of photoelectrons, respectively.

To gain deeper insight into the momentum-resolved spin-polarized photoelectrons, we calculate the 1D distributions of the spin-up and spin-down photoelectrons as a function of the photoelectron kinetic energy $E_{\rm kin}$, the elevation angle θ, and the azimuthal angle ϕ, according to $Y_\pm^r(\sqrt{2E_{\rm kin}})$, $Y_\pm^\theta(\theta) = \iint Y_\pm(\mathbf{p}) p_r^2 \cos\theta dp_r d\phi$, and $Y_\pm^\phi(\phi) = \iint Y_\pm(\mathbf{p}) p_r^2 \cos\theta dp_r d\theta$, respectively. The results for three different pulse intensities, $I_1 = 1.75 \times 10^{14}\,\mathrm{W/cm^2}$, $I_2 = 1.5 \times 10^{14}\,\mathrm{W/cm^2}$, and $I_3 = 1.25 \times 10^{14}\,\mathrm{W/cm^2}$ (indicated by the thickness of the curves), are shown in Figs. 4(a)–4(c). The spin polarization of photoelectrons is calculated as

$$\mathcal{P} = \frac{Y^\uparrow - Y^\downarrow}{Y^\uparrow + Y^\downarrow}, \tag{3}$$

and the corresponding distributions are shown in Figs. 4(d)–4(f).

First, as shown in Fig. 4(a), the kinetic energy of the spin-down photoelectron released from the corotating orbital is larger than that of the spin-up photoelectron released from the counterrotating orbital. The underlying physics has already been discussed above and shown in Fig. 2(c). The peak positions of the spectra in Fig. 4(a) for the spin-up and spin-down photoelectrons are 10.54 and 14.72 eV for I_1, 9.04 and 13.33 eV for I_2, and 7.55 and 11.77 eV for I_3, respectively. These energy differences in the spectra for spin-up and spin-down photoelectrons lead ultimately to the strong energy dependence of the spin polarization ranging from +96% to −58%, as shown in Fig. 4(d). The zero crossings of the spin polarization for I_1, I_2, and I_3 are located at 21.82, 20.30, and 18.83 eV, respectively, and are shifted to lower kinetic energy with decreasing pulse intensity. For dominant ionization, the spin polarizations at peak positions of the spectra for the spin-up photoelectrons are 75%, 78%, and 81% for intensities I_1, I_2, and I_3, respectively.

Second, from Fig. 4(b) we can see that the elevation angles with respect to the peaks of the distribution for the spin-up photoelectron (located at $\theta \approx \pm 15^\circ$) have an obvious offset from those for the spin-down photoelectron (located at $\theta \approx \pm 12^\circ$). This can be understood from the 2D PMDs $Y_\pm(p_\rho, p_z)$ shown in Figs. 3(d) and 3(e). The momentum drifts along p_z are similar for both cases, but the spin-up photoelectron has a smaller momentum drift along p_ρ, as shown in Fig. 3(e). Thus, the elevation angle, defined as $\theta = \arctan\frac{p_z}{p_\rho}$, for the emitting spin-up photoelectron is larger than that for the emitting spin-down photoelectron. Moreover, due to the higher ionization yield of the spin-up photoelectron, we can see from Fig. 3(f) that the distribution of the spin-up polarization is broader. This leads to the strong dependence of the spin polarization on the elevation angle, as shown in Fig. 4(e). The spin polarization reaches the maximum +92% located at $\theta \approx \pm 42^\circ$, where the production of spin-up photoelectrons becomes dominant. Although the spin polarization generally decreases with increasing kinetic energy, the spin polarizations at these two specific emitting angles are enhanced in the

entire range of the kinetic energy. According to our simulation results for I_1, for a kinetic energy of around 20 eV, the spin polarizations at $\theta \approx \pm 42^\circ$ are about 80%, which is obviously much larger than the angle-integrated spin polarization shown in Fig. 4(d). Furthermore, at emitting angles $\theta \approx \pm 42^\circ$, the ionization yields become dominant at a kinetic energy of 7.97 eV, and the corresponding spin polarization is 96%.

Finally, due to the Coulomb effect, the peaks of the ϕ-dependent distributions of the photoelectrons are slightly deflected from $\phi = 90^\circ$, which has been observed in attoclock experiments [29]. For NO, the offset azimuthal angle of the spin-up photoelectron is approximately 3° larger than that of the spin-down photoelectron because the spin-up photoelectron has a smaller kinetic energy and it spends more time interacting with the Coulomb potential. However, the variation of the azimuthal angle ϕ has merely a weak effect on the spin polarization, as shown in Fig. 4(f), because it is associated with only the varying instant field strength of the few-cycle CP laser pulse along the ϕ coordinate. As already predicted in Ref. [44], the spin polarization is high for low laser intensities, and it is in accordance with the slightly larger spin polarization at $\phi = 270^\circ$ than at $\phi = 90^\circ$. Figure 4(f) also shows, in accordance with our prediction, that the spin polarization in the whole range of the azimuthal angle increases with decreasing pulse intensity. The average spin polarization of photoelectrons, according to Eq. (3) for total ionization yields, is 52%, 55%, and 58% for I_1, I_2, and I_3, respectively.

IV. CONCLUSION

In summary, we have predicted that the spin polarization of photoelectrons produced by nonadiabatic ionization of current-carrying orbitals in strong circularly polarized laser fields can be enhanced by filtering the momentum and the emitting angle of photoelectrons in experiments. For the ensemble of NO starting from the ground state $|\Pi_{1/2}\rangle$ with one electron in the doubly degenerate valence π shell, the momentum-resolved spin polarization can reach values above 90% for slow photoelectrons and also for electrons emitted at angles $\pm 42^\circ$ that are measured from the polarization plane. Our study clearly shows that the momentum-resolved spin polarization can be much larger than the average spin polarization (in our case between 50% and 60%) that is controlled only by the laser pulse. Thus, besides the laser control, the use of the momentum gate in strong-field experiments will enhance the spin polarization of photoelectrons. Such full control of femtosecond spin-polarized electron pulses by varying not only the laser parameters but also the photoelectron momentum and its emitting angle is advantageous for experimental investigations of ultrafast spin-resolved processes in physics, chemistry, and biology, for example, the ultrafast detection of magnetic properties and chirality of materials and molecules. In particular, spin-polarized electrons are used for imaging magnetic microstructures at surfaces and in thin films [53], and those produced by short pulses can be further used for time-resolved magnetic imaging.

ACKNOWLEDGMENTS

This work was financially supported by the Max Planck Society for the Max Planck Research Group "Current-Carrying Quantum Dynamics" (CCQD) and by the Deutsche Forschungsgemeinschaft, Priority Programme 1840 "Quantum Dynamics in Tailored Intense Fields" (QUTIF).

APPENDIX: FINITE-DIFFERENCE COEFFICIENTS

To facilitate the derivation of the formula for finite-difference coefficients, we consider the 1D wave function $\psi_j = \psi(x_j)$ [as the cut of the 3D wave function $\psi(x_j, y, z)$ at fixed values y and z] distributed on a nonuniform grid with grid points x_j ($j = 1, \ldots, J$). Using the five-point central finite-difference method, the second-order derivative of ψ_j is written as

$$\partial_x^2 \psi_j = C_1^j \psi_{j-2} + C_2^j \psi_{j-1} + C_3^j \psi_j + C_4^j \psi_{j+1} + C_5^j \psi_{j+2}, \tag{A1}$$

with five coefficients C_s^j ($s = 1, \ldots, 5$) that, in general, depend on the grid index j.

To interpolate the wave function ψ_j on a nonuniform grid, we use the interpolation polynomial in the Lagrange form for a set of K data points (x_k, ψ_k) ($k = 1, \ldots, K$), and it is given by [54]

$$L(x) := \sum_{k=1}^{K} \psi_k l_k(x), \tag{A2}$$

with

$$l_k(x) := \prod_{\substack{1 \leqslant m \leqslant K \\ m \neq k}} \frac{x - x_m}{x_k - x_m}. \tag{A3}$$

Then, the second-order derivative at a certain grid point x_c is obtained from

$$L''(x)\big|_{x=x_c} = \sum_{k=1}^{K} \psi_k \, l_k''(x)\big|_{x=x_c}. \tag{A4}$$

By comparing Eq. (A4) with Eq. (A1), we find that the coefficients C_s^j ($s = 1, \ldots, 5$) in Eq. (A1) correspond to the values of $l_k''(x)$ ($k = 1, \ldots, 5$) at $x = x_3$ with $K = 5$ in Eq. (A4).

The second-order derivative of $l_k(x)$ is calculated straightforwardly from Eq. (A3), and its general expressions are

$$l_k''(x) = \left(\prod_{\substack{1 \leqslant m \leqslant K \\ m \neq k}} \frac{1}{(x_k - x_m)} \right) \times \sum_{\substack{1 \leqslant q \leqslant K \\ q \neq k}} \left[\sum_{\substack{1 \leqslant p \leqslant K \\ p \notin \{k,q\}}} \left(\prod_{\substack{1 \leqslant m \leqslant K \\ m \notin \{k,p,q\}}} (x - x_m) \right) \right] \tag{A5}$$

for $K \geqslant 4$ and

$$l_k''(x) = 2 \prod_{\substack{1 \leqslant m \leqslant 3 \\ m \neq k}} \frac{1}{(x_k - x_m)} \tag{A6}$$

for $K = 3$. Therefore, based on the chosen grid points and the order of the finite-difference method, we obtain the corresponding coefficients from Eq. (A5) or (A6). For

example, in the special case of the uniform step size Δx, we get for $K = 5$ the coefficients $\{-1/12, 4/3, -5/2, 4/3, -1/12\}/\Delta x^2$ from Eq. (A5) and use them as the five-point finite-difference coefficients in Eq. (A1), which are independent of the grid index j due to the uniformity of the grid. If three points ($K = 3$) are used for the central finite-difference method, we obtain from Eq. (A6) the well-known coefficients $\{1, -2, 1\}/\Delta x^2$. In this case, the procedure returns to the common Crank-Nicolson method. One can also obtain from Eq. (A5) the coefficients for seven-point or even higher-order central finite-difference methods, but then Eq. (A1) needs to be rewritten correspondingly.

[1] J. L. Krause, K. J. Schafer, and K. C. Kulander, Phys. Rev. Lett. **68**, 3535 (1992).
[2] P. B. Corkum, Phys. Rev. Lett. **71**, 1994 (1993).
[3] G. Vampa, C. R. McDonald, G. Orlando, D. D. Klug, P. B. Corkum, and T. Brabec, Phys. Rev. Lett. **113**, 073901 (2014).
[4] M. Wu, S. Ghimire, D. A. Reis, K. J. Schafer, and M. B. Gaarde, Phys. Rev. A **91**, 043839 (2015).
[5] E. Goulielmakis, M. Schultze, M. Hofstetter, V. S. Yakovlev, J. Gagnon, M. Uiberacker, A. L. Aquila, E. M. Gullikson, D. T. Attwood, R. Kienberger, F. Krausz, and U. Kleineberg, Science **320**, 1614 (2008).
[6] K. Zhao, Q. Zhang, M. Chini, Y. Wu, X. Wang, and Z. Chang, Opt. Lett. **37**, 3891 (2012).
[7] E. J. Takahashi, P. Lan, O. D. Mücke, Y. Nabekawa, and K. Midorikawa, Nat. Commun. **4**, 2691 (2013).
[8] W. Becker, X. Liu, P. J. Ho, and J. H. Eberly, Rev. Mod. Phys. **84**, 1011 (2012).
[9] C. Faria and X. Liu, J. Mod. Opt. **58**, 1076 (2011).
[10] M. F. Kling, C. Siedschlag, A. J. Verhoef, J. I. Khan, M. Schultze, T. Uphues, Y. Ni, M. Uiberacker, M. Drescher, F. Krausz, and M. J. J. Vrakking, Science **312**, 246 (2006).
[11] K. Liu, Q. Zhang, P. Lan, and P. Lu, Opt. Express **21**, 5107 (2013).
[12] X. Gong, P. He, Q. Song, Q. Ji, H. Pan, J. Ding, F. He, H. Zeng, and J. Wu, Phys. Rev. Lett. **113**, 203001 (2014).
[13] T. Morishita, A.-T. Le, Z. Chen, and C. D. Lin, Phys. Rev. Lett. **100**, 013903 (2008).
[14] M. Meckel, D. Comtois, D. Zeidler, A. Staudte, D. Pavičić, H. C. Bandulet, H. Pépin, J. C. Kieffer, R. Dörner, D. M. Villeneuve, and P. B. Corkum, Science **320**, 1478 (2008).
[15] M. G. Pullen, B. Wolter, A.-T. Le, M. Baudisch, M. Sclafani, H. Pires, C. D. Schröter, J. Ullrich, R. Moshammer, T. Pfeifer, C. D. Lin, and J. Biegert, Nat. Commun. **7**, 11922 (2016).
[16] Y. Zhou, O. I. Tolstikhin, and T. Morishita, Phys. Rev. Lett. **116**, 173001 (2016).
[17] N. Rohringer and R. Santra, Phys. Rev. A **79**, 053402 (2009).
[18] O. Smirnova, Y. Mairesse, S. Patchkovskii, N. Dudovich, D. Villeneuve, P. Corkum, and M. Y. Ivanov, Nature (London) **460**, 972 (2009).
[19] A. E. Boguslavskiy, J. Mikosch, A. Gijsbertsen, M. Spanner, S. Patchkovskii, N. Gador, M. J. J. Vrakking, and A. Stolow, Science **335**, 1336 (2012).
[20] T. Sato and K. L. Ishikawa, Phys. Rev. A **88**, 023402 (2013).
[21] H. Miyagi and L. B. Madsen, Phys. Rev. A **95**, 023415 (2017).
[22] F. Krausz and M. Ivanov, Rev. Mod. Phys. **81**, 163 (2009).
[23] N. Takemoto and A. Becker, Phys. Rev. Lett. **105**, 203004 (2010).
[24] S. Skruszewicz, J. Tiggesbäumker, K.-H. Meiwes-Broer, M. Arbeiter, T. Fennel, and D. Bauer, Phys. Rev. Lett. **115**, 043001 (2015).
[25] M. M. Liu, M. Li, C. Wu, Q. Gong, A. Staudte, and Y. Liu, Phys. Rev. Lett. **116**, 163004 (2016).
[26] K. Liu, P. Lan, C. Huang, Q. Zhang, and P. Lu, Phys. Rev. A **89**, 053423 (2014).
[27] C. I. Blaga, F. Catoire, P. Colosimo, G. G. Paulus, H. G. Muller, P. Agostini, and L. F. DiMauro, Nat. Phys. **5**, 335 (2009).
[28] W. Quan, Z. Lin, M. Wu, H. Kang, H. Liu, X. Liu, J. Chen, J. Liu, X. T. He, S. G. Chen, H. Xiong, L. Guo, H. Xu, Y. Fu, Y. Cheng, and Z. Z. Xu, Phys. Rev. Lett. **103**, 093001 (2009).
[29] P. Eckle, A. N. Pfeiffer, C. Cirelli, A. Staudte, R. Dörner, H. G. Muller, M. Büttiker, and U. Keller, Science **322**, 1525 (2008).
[30] L. Torlina, F. Morales, J. Kaushal, I. Ivanov, A. Kheifets, A. Zielinski, A. Scrinzi, H. G. Muller, S. Sukiasyan, M. Ivanov, and O. Smirnova, Nat. Phys. **11**, 503 (2015).
[31] N. Teeny, E. Yakaboylu, H. Bauke, and C. H. Keitel, Phys. Rev. Lett. **116**, 063003 (2016).
[32] H. Ni, U. Saalmann, and J.-M. Rost, Phys. Rev. Lett. **117**, 023002 (2016).
[33] I. Barth and O. Smirnova, Phys. Rev. A **88**, 013401 (2013).
[34] D. B. Milošević, Phys. Rev. A **93**, 051402(R) (2016).
[35] A. Hartung, F. Morales, M. Kunitski, K. Henrichs, A. Laucke, M. Richter, T. Jahnke, A. Kalinin, M. Schöffler, L. P. H. Schmidt, M. Ivanov, O. Smirnova, and R. Dörner, Nat. Photonics **10**, 526 (2016).
[36] A. V. Subashiev, Y. A. Mamaev, Y. P. Yashin, and J. E. Clendenin, Phys. Low Dimens. Struct. **1–2**, 1 (1999).
[37] R. Naaman and D. H. Waldeck, Annu. Rev. Phys. Chem. **66**, 263 (2015).
[38] K. Michaeli, N. Kantor-Uriel, R. Naaman, and D. H. Waldeck, Chem. Soc. Rev. **45**, 6478 (2016).
[39] I. Barth and O. Smirnova, Phys. Rev. A **84**, 063415 (2011); **85**, 029906(E) (2012); **85**, 039903(E) (2012).
[40] I. Barth and O. Smirnova, Phys. Rev. A **87**, 013433 (2013).
[41] I. Barth and M. Lein, J. Phys. B **47**, 204016 (2014).
[42] X. Zhu, P. Lan, K. Liu, Y. Li, X. Liu, Q. Zhang, I. Barth, and P. Lu, Opt. Express **24**, 4196 (2016).
[43] T. Herath, L. Yan, S. K. Lee, and W. Li, Phys. Rev. Lett. **109**, 043004 (2012).
[44] K. Liu and I. Barth, Phys. Rev. A **94**, 043402 (2016).
[45] K. Liu and I. Barth, J. Mod. Opt. **64**, 987 (2017).
[46] P. M. Kraus, S. B. Zhang, A. Gijsbertsen, R. R. Lucchese, N. Rohringer, and H. J. Wörner, Phys. Rev. Lett. **111**, 243005 (2013).
[47] J. Kaushal, F. Morales, and O. Smirnova, Phys. Rev. A **92**, 063405 (2015).
[48] Y. Li, P. Lan, H. Xie, M. He, X. Zhu, Q. Zhang, and P. Lu, Opt. Express **23**, 28801 (2015).

[49] N. Watanabe and M. Tsukada, Phys. Rev. E **62**, 2914 (2000).
[50] X. M. Tong, K. Hino, and N. Toshima, Phys. Rev. A **74**, 031405(R) (2006).
[51] A. Karamatskou, S. Pabst, Y. J. Chen, and R. Santra, Phys. Rev. A **89**, 033415 (2014).
[52] I. Petersen, J. Henkel, and M. Lein, Phys. Rev. Lett. **114**, 103004 (2015).
[53] N. Rougemaille and A. K. Schmid, Eur. Phys. J. Appl. Phys. **50**, 20101 (2010).
[54] E. Meijering, Proc. IEEE **90**, 319 (2002).